

EFFECTS OF MICROSTRUCTURE ON MECHANICAL PROPERTIES OF QUASICRYSTALLINE Al–Ni–Fe ALLOYS

O. SUKHOVA

Institute of Transport Systems and Technologies of National Academy of Sciences
of Ukraine Pisarzhevsky St. 5, 49005 Dnipro, Ukraine
E-mail: sukhovaya@ukr.net

Received January 20, 2023

Abstract. The effects of microstructure on the mechanical properties of as-cast $\text{Al}_{72}\text{Ni}_{13}\text{Fe}_{15}$ and $\text{Al}_{72}\text{Ni}_{23}\text{Fe}_5$ alloys were investigated. These alloys were composed of decagonal quasicrystalline D-phase coexisting with Al-based intermetallics. The mechanical properties were characterized by means of microhardness indentation at room temperature. Fracture mode was examined by scanning electron microscopy. The ductility of the alloys tended to decrease with increasing iron content.

Key words: quasicrystalline Al–Ni–Fe alloys, mechanical properties, fracture mode.

1. INTRODUCTION

Quasicrystalline alloys are considered as new materials with enhanced properties such as very high hardness, low toughness, and a high capability for elastic recovery due to their unique atomic arrangement [1–4]. However, the use of the quasicrystalline alloys is limited due to their high brittleness at room temperature [5, 6]. Whereas at high temperature, they show ductility due to the mobility of thermally activated distributions.

Among the various types of quasicrystals, the decagonal (D) quasicrystals of Al–Ni–Fe alloys have been studied quite extensively [7–15]. The D-phase is quasiperiodic in two and periodic in the other dimension [16, 17]. Most of the studies on Al–Ni–Fe alloys focus on the quasicrystalline structure and physical properties [18–20]. In addition, studies on the equilibrium phase diagram, the effects of annealing, and the orientation dependence on decagonal phase growth have been conducted [21–23]. However, the mechanical properties of quasicrystals are seldom reported.

It has been known that the change of the microstructure influences mechanical properties [24–28]. Therefore, the microstructure effect on fracture mechanisms is actively studied by many researchers [29–34]. Apart from the inherent advantages of quasicrystalline alloys, their microstructure determined by alloy composition also plays an important role in service performance [35–39]. Considering their potential application, the understanding of the failure mechanisms of quasicrystalline alloys is necessary to predict their service performance. By adjusting the microstructure, the fracture mechanism could be controlled [40–42].

Further research in this direction is required for making use of the properties of quasicrystalline alloys for some technological applications. The aim of the present study is to investigate the mechanical properties of the quasicrystalline Al–Ni–Fe alloys fabricated by a slow-cooling method by means of a hardness indentation technique and to reveal features of their fracture mechanisms.

2. EXPERIMENTAL

Quasicrystalline Al–Ni–Fe alloys were prepared by melting mixtures of 99.9% pure elements in Tamman furnace ($V_{\text{cool}}=5$ K/s). The compositions of the alloys used in this research were selected from the ternary Al–Ni–Fe phase diagram [21–23]. Finally, the selected quasicrystalline alloys had a stoichiometry of $\text{Al}_{72}\text{Ni}_{13}\text{Fe}_{15}$ and $\text{Al}_{72}\text{Ni}_{23}\text{Fe}_5$ determined by atomic absorption spectroscopy (AAS, SPRUT SEF-01-M).

Samples were mechanically polished and etched for optical microscopy (OM, NEOPHOT). The chemical compositions of each phase were identified by X-ray diffraction (XRD, DRON-UM-1, Cu- K_{α} source) and energy dispersive spectroscopy (EDS, REMMA 102-02). Based on the results of XRD and EDS, the different colored regions on a scanning electron microscope (SEM, REMMA 102-02) backscattering images were matched to the phases identified by XRD. To calculate the volume fraction of each phase, image analyzer (IA, EPIQUANT) was used for image processing and obtaining the area of each phase. Differential thermal analysis (DTA, Q-1500 D) was also done to determine the melting points of the phases at a heating rate of 0.35 K/s. The temperature of DTA equipment was controlled using a PtRh-Pt thermocouple.

Microhardness (H_V) measurements were made using a PMT-3 Vickers tester at room temperature for a loading time of 15 s under the loads varying from 50 g to 200 g. Values of the microhardness were averaged from 10 measurements. The fracture toughness (K_{IC}) of the samples was also obtained by the Vickers indenter by measuring crack length around the indentation [43]. Fracture toughness measurements were carried out ten times each to provide repeatability with standard deviations. Young's modulus (E) of complex Al-based intermetallics was calculated from their melting points using the formula given in [44].

To investigate fractographic behavior, the load was applied to cause a failure of the selected specimens by crushing, and then fracture profiles were compared and evaluated with a scanning electron microscope (SEM, REM-106I) to further examine the fracture mechanisms [45–47].

3. RESULTS AND DISCUSSION

Figures 1 a,b show the solidification microstructure of the $\text{Al}_{72}\text{Ni}_{13}\text{Fe}_{15}$ alloy formed during conventional casting [11]. Two phases observed are Al_5FeNi and

quasicrystalline D-phase constituted about 35% of the volume of the specimen, all main reflections of which are seen in the X-ray diffractogram (Fig. 1c). The identification of each phase is also supported by the DTA analysis (Table 1).

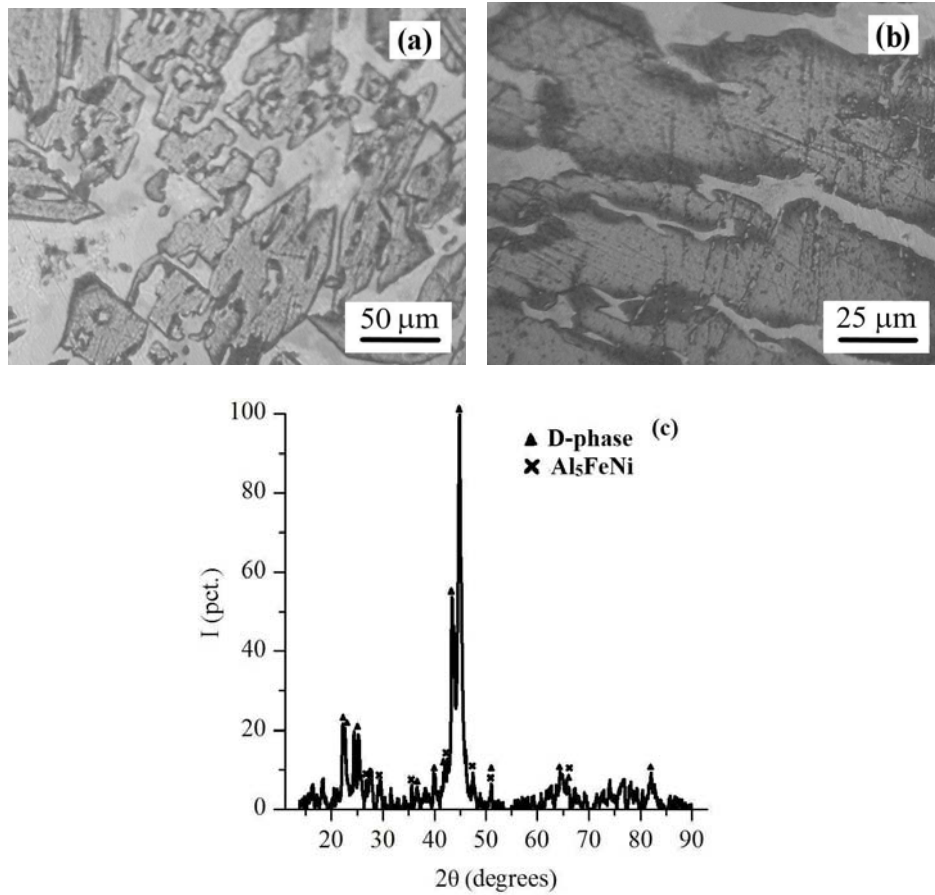


Fig. 1 – OM images (a,b) and XRD pattern (c) of the $\text{Al}_{72}\text{Ni}_{13}\text{Fe}_{15}$ alloy.

Table 1

Melting points (T_m), microhardness (H_V) and Young's modulus (E) of identified phases

Alloys	Phase constituents	T_m [K]	H_V [GPa]	E [GPa]
$\text{Al}_{72}\text{Ni}_{13}\text{Fe}_{15}$	Al_5FeNi	1320 ± 3	7.2 ± 0.1	94.8 ± 0.4
	D-phase	1198 ± 5	10.9 ± 0.3	79.8 ± 0.6
$\text{Al}_{72}\text{Ni}_{23}\text{Fe}_5$	$\text{Al}_3(\text{Ni,Fe})_2$	1340 ± 3	6.5 ± 0.3	97.2 ± 0.2
	D-phase	1210 ± 4	10.2 ± 0.2	81.2 ± 0.4
	$\text{Al}_{13}(\text{Ni,Fe})_4$	1138 ± 4	6.0 ± 0.4	72.4 ± 0.5
	$\text{Al}_3(\text{Ni,Fe})$	1138 ± 4	6.1 ± 0.3	72.4 ± 0.5

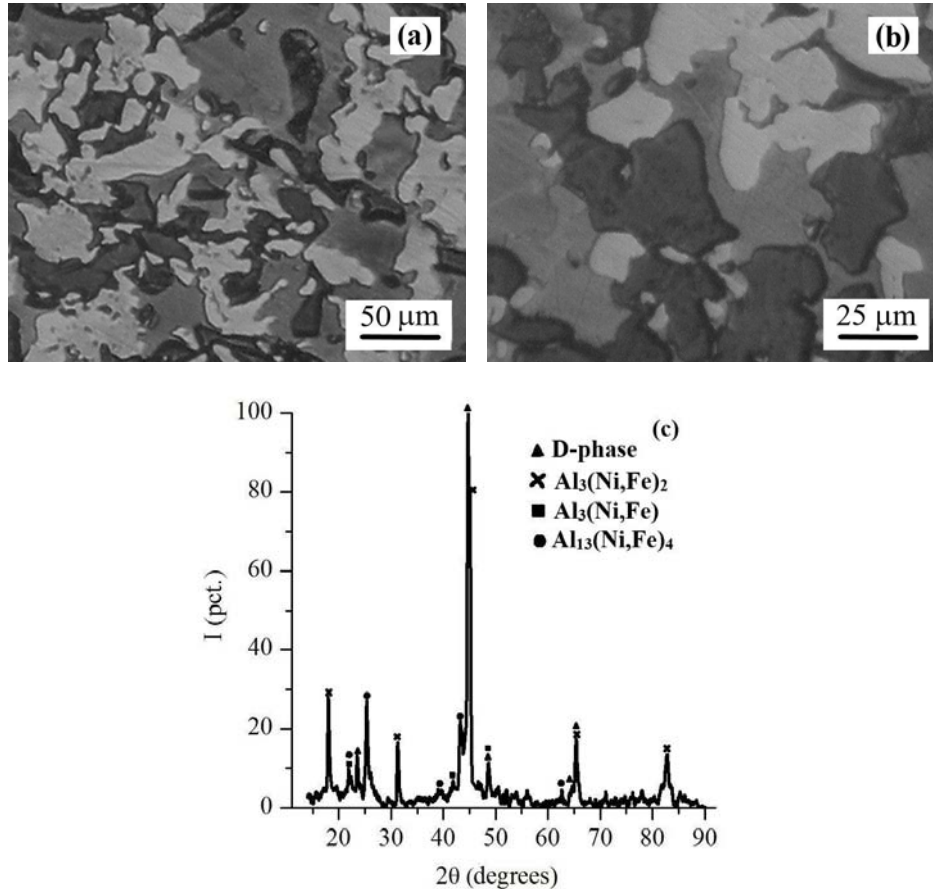


Fig. 2 – OM images (a, b) and XRD pattern (c) of the Al₇₂Ni₂₃Fe₅ alloy.

Examination by light-optical microscope as well as by diffractometer of the Al₇₂Ni₂₃Fe₅ alloy reveals multiphase structure (Fig. 2a,b) [9]. There exist at least four different phases, discernible by the image contrast, namely D-phase, Al₁₃(Ni,Fe)₄, Al₃(Ni,Fe)₂, and Al₃(Ni,Fe). Figure 2c shows the corresponding X-ray diffraction pattern from the Al₇₂Ni₂₃Fe₅ alloy. Based on these observations, it is found that this alloy has lower volume fraction of the quasicrystalline D-phase (about 15 vol.%). As Ni is added up to 23 at.%, replacing the Fe atoms, the crystallization mode of the Al₇₂Ni₂₃Fe₅ alloy changes from two to three stages. The extra exothermic peak at the lower temperature 1138 K appears due to the decomposition of the quasicrystalline D-phase to Al₁₃(Ni,Fe)₄, Al₃(Ni,Fe)₂, and Al₃(Ni,Fe) phases upon cooling (Table 1).

Table 1 also summarizes the microhardness measured at a load of 50 g and Young's modulus of the identified phases. Considering microhardness and Young's modulus as additive characteristics, average H_V value decreases from 8.5 GPa to

7.0 GPa and average E value slightly increases from 89.5 GPa to 90.6 GPa for the $\text{Al}_{72}\text{Ni}_{13}\text{Fe}_{15}$ and $\text{Al}_{72}\text{Ni}_{23}\text{Fe}_5$ alloys correspondingly, which evidences that alloy containing less iron shows lower brittleness.

The microhardness values of the investigated Al–Ni–Fe alloys having different D-phase content at various loads are listed in Table 2. The $\text{Al}_{72}\text{Ni}_{23}\text{Fe}_5$ alloy reveals the lower average microhardness value 6.73 GPa (0.28 deviation) that ranges from 6.44 to 7.0 GPa. The microhardness of the $\text{Al}_{72}\text{Ni}_{13}\text{Fe}_{15}$ alloy shows an average of 7.95 GPa (0.51 deviation) between 7.50 and 8.51 GPa. The microhardness for both the studied alloys is found to decrease with the load increasing. The obtained load dependency of microhardness values may be explained by surface resistance mainly from elastic deformation [48]. In the lower load region, the surface resistance is comparable with the applied load, which results in higher microhardness. On the contrary, at higher loads the surface resistance is negligible, thus decreasing the microhardness value.

Table 2

Values of microhardness (H_V) and fracture toughness (K_{1C}) as a function of applied load

Load [g]	$\text{Al}_{72}\text{Ni}_{13}\text{Fe}_{15}$ alloy		$\text{Al}_{72}\text{Ni}_{23}\text{Fe}_5$ alloy	
	H_V [GPa]	K_{1C} [$\text{MPa}\cdot\text{m}^{1/2}$]	H_V [GPa]	K_{1C} [$\text{MPa}\cdot\text{m}^{1/2}$]
50	8.51 ± 0.37	no cracks	7.0 ± 0.32	no cracks
100	8.15 ± 0.12	2.82 ± 0.11	6.84 ± 0.16	no cracks
150	7.63 ± 0.20	3.14 ± 0.21	6.62 ± 0.23	4.37 ± 0.10
200	7.50 ± 0.11	3.65 ± 0.14	6.44 ± 0.10	4.58 ± 0.16

With regards to the microhardness test, the cracks occur at the edge of the indentation of the $\text{Al}_{72}\text{Ni}_{13}\text{Fe}_{15}$ alloy when the applied load is larger than 50 g. As the load is increased up to 150 g, the radial cracks from the corner of the indentation also develop. As for the $\text{Al}_{72}\text{Ni}_{23}\text{Fe}_5$ alloy, the obvious cracks near the corner of the indenter mark are observed when the load is increasing up to 150 g, and radial cracks appear at a load of 200 g, which suggests that this alloy has better ductility.

The determined values of fracture toughness are presented in Table 2. It reveals that the fracture toughness of the $\text{Al}_{72}\text{Ni}_{23}\text{Fe}_5$ alloy is higher than that of the $\text{Al}_{72}\text{Ni}_{13}\text{Fe}_{15}$ alloy, indicating the greater brittleness of the latter. The average fracture toughness value for the $\text{Al}_{72}\text{Ni}_{13}\text{Fe}_{15}$ alloy is found to be around $3.2 \text{ MPa}\cdot\text{m}^{1/2}$ (0.30 deviation), and that for the $\text{Al}_{72}\text{Ni}_{23}\text{Fe}_5$ alloy is $4.5 \text{ MPa}\cdot\text{m}^{1/2}$ (0.11 deviation). There is a tendency for fracture toughness to increase with an increase in load value. It is obvious that microhardness and fracture toughness are in inverse relationship.

Tables 1 and 2 clearly show that there is a strong inverse proportion between crystalline phases concentration (fracture toughness) and quasicrystalline D-phase concentration (hardness). From this, it may be concluded that higher iron content reduces the ductility of the investigated Al–Ni–Fe alloys.

Figure 3 shows the fracture surface of the $\text{Al}_{72}\text{Ni}_{13}\text{Fe}_{15}$ alloy that is reasonably smooth, which reveals the typical brittle failure mechanism. Cracks propagate

primarily in an intergranular mode, which indicates that the grain boundary regions can be embrittled by the flaws. Therefore, the bonds between alloy grains are weaker than the alloy itself at room temperature. The D-phase accelerates crack propagation due to its little or no plastic deformation prior to fracture (Fig. 3a,b). In contrast, a smaller fracture is observed in the Al_5FeNi phase (Fig. 3c,d). The brittleness of these phases can be explained by the complex atomic arrangement as well as ionic and covalent bonds in them. Besides, two-phase coarse microstructure of the $\text{Al}_{72}\text{Ni}_{13}\text{Fe}_{15}$ alloy can favor crack propagation. That is why this alloy exhibits little plasticity in the experiments.

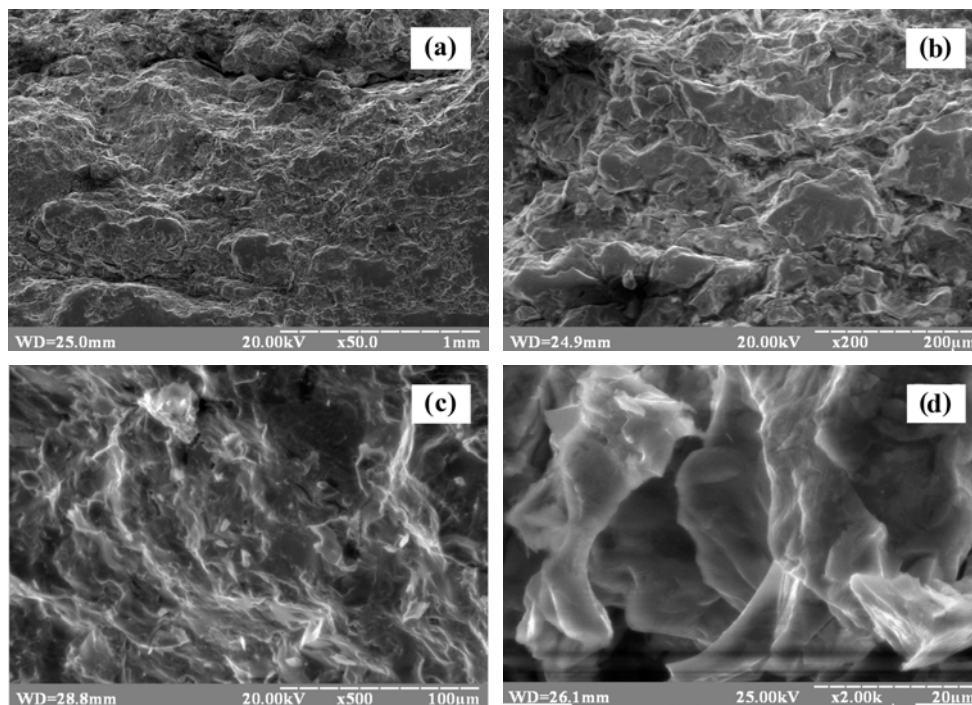


Fig. 3 – SEM-micrographs of the fracture surface of the $\text{Al}_{72}\text{Ni}_{13}\text{Fe}_{15}$ alloy.

The $\text{Al}_{72}\text{Ni}_{23}\text{Fe}_5$ alloy exhibits two types of fracture behavior: mainly brittle fracture of D-phase and $\text{Al}_3(\text{Ni,Fe})_2$ phase (Fig. 4a,b) and mixed-mode fracture of $\text{Al}_{13}(\text{Ni,Fe})_4$ and $\text{Al}_3(\text{Ni,Fe})$ phases combining features of brittle and ductile failure (Fig. 4c,d). It is difficult to consider that the quasicrystalline D-phase itself in the studied alloy has plastic deformability. Its brittle fracture surface shows a flat topography with some traces of ductile failure. The better mechanical properties of the $\text{Al}_{72}\text{Ni}_{23}\text{Fe}_5$ alloy may be attributed to its fine multiphase structure that tends to mitigate crack initiation and to reduce the possibility of brittle fracture. Therefore, the $\text{Al}_{72}\text{Ni}_{23}\text{Fe}_5$ alloy possesses favorable hardness and fracture toughness, which leads to improved failure resistance.

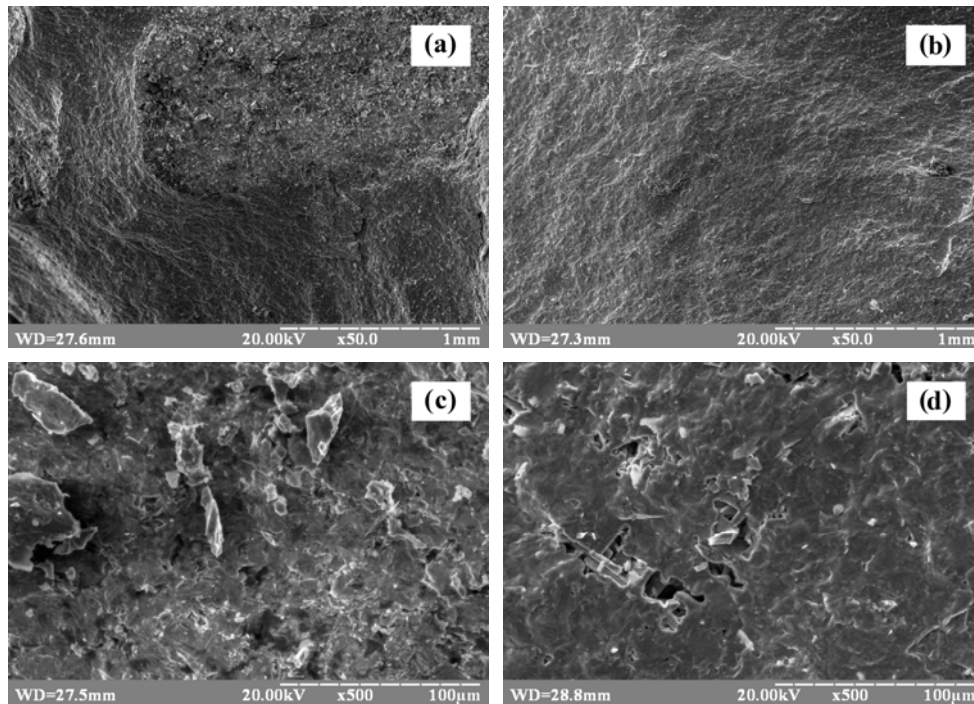


Fig. 4 – SEM-micrographs of the fracture surface of the $\text{Al}_{72}\text{Ni}_{23}\text{Fe}_5$ alloy.

4. CONCLUSIONS

In this research, two- and four-phase $\text{Al}_{72}\text{Ni}_{13}\text{Fe}_{15}$ and $\text{Al}_{72}\text{Ni}_{23}\text{Fe}_5$ alloys correspondingly with different quasicrystalline D-phase content have been studied. The $\text{Al}_{72}\text{Ni}_{13}\text{Fe}_{15}$ alloy shows an enhanced hardness due to the higher content of D-phase and mechanical properties of the dominant Al_5FeNi phase. Ni addition instead of Fe leads to an increase in fracture toughness and Young's modulus of the $\text{Al}_{72}\text{Ni}_{23}\text{Fe}_5$ alloy. So, there is a tendency for ductility to increase with decreasing Fe content of the alloys.

As applied load is increased, the microhardness of both the alloys decreases, but fracture toughness increases. The decrease in iron content of the alloys leads to least effect of load on values of microhardness and fracture toughness.

The appearance of the fracture surfaces of the $\text{Al}_{72}\text{Ni}_{13}\text{Fe}_{15}$ and $\text{Al}_{72}\text{Ni}_{23}\text{Fe}_5$ alloys is found to be consistent with the iron content. Fracture of the $\text{Al}_{72}\text{Ni}_{13}\text{Fe}_{15}$ alloy containing more iron occurs through a brittle mode. The failure process is dominated by intergranular fracture mechanism. The failure mode of the $\text{Al}_{72}\text{Ni}_{23}\text{Fe}_5$ alloy with lower iron content is mainly brittle but the traces of ductile fracture are found as well. This is because the $\text{Al}_{13}(\text{Ni},\text{Fe})_4$ and $\text{Al}_3(\text{Ni},\text{Fe})$ phases, which fail in mix-mode manner, are more resistant to cracking and decrease brittle

fracture. Therefore, the four-phase quasicrystalline $\text{Al}_{72}\text{Ni}_{23}\text{Fe}_5$ alloy, combining both brittle and ductile failure mechanisms, exhibits a better fracture resistance in comparison with the two-phase $\text{Al}_{72}\text{Ni}_{13}\text{Fe}_{15}$ alloy that fails by brittle mode.

REFERENCES

1. N. K. Mukhopadhyay and T. P. Yadav, *J. Indian. Inst. Sci.* **102**, 59–90 (2022).
2. E. Maciá-Barber, *Quasicrystals: Fundamentals and Applications*, Taylor & Francis CRC Press, London-New York, 2020.
3. O. V. Sukhova and K. V. Ustinova, *Funct. Mater.* **3**, 495–506 (2019).
4. S. I. Ryabtsev, V. A. Polonsky, and O. V. Sukhova, *Mater. Sci.* **2**, 263–272 (2020).
5. H. R. Trebin, *Quasicrystals: Structure and Physical Properties*, Wiley-VCH Verlag GmbH & Co., Weinheim, 2003.
6. J.-M. Dubois, *Chem. Soc. Rev.* **41**, 6760–6777 (2012).
7. O. V. Sukhova, V. A. Polonsky, and K. V. Ustinova, *Metallofiz. Noveishie Tekhnologii* **11**, 1475–1487 (2018).
8. F. Nejdassattari, Z. M. Stadnik, J. Przewoznik, and B. Grushko, *J. Alloys Compd.* **1–2**, 612–620 (2016).
9. O. V. Sukhova, V. A. Polonsky, and K. V. Ustinova, *Vopr. Khimii Khimicheskoi Tekhnologii* **3**, 46–52 (2019).
10. A. D. Setyawan, D. V. Louzguine, K. Sasamori, H. M. Kimura, S. Ranganathan, and A. Inoue, *J. Alloys Compd.* **1–2**, 132–138 (2005).
11. O. V. Sukhova and V. A. Polonsky, *East Eur. J. Phys.* **3**, 5–10 (2020).
12. K. Hiraga and K. T. Park, *J. Mater. Res.* **7**, 1702–1705 (1996).
13. W. Wolf, C. Bolfarini, C. S. Kiminami, and W. J. Botta, *J. Alloys Compd.* **1–2**, 1–6 (2020).
14. J.-B. Qiang, D.-H. Wang, and C. M. Bao, *J. Mater. Res.* **9**, 2653–2660 (2001).
15. B. Grushko, U. Lemmerz, K. Fischer, and C. Freiburg, *Phys. Stat. Sol.* **17**, 17–30 (1996).
16. Y. Zou, P. Kuczera, and J. Wolny, *Acta Phys. Pol. A* **4**, 845–847 (2016).
17. L. Bindi, N. Yao, C. Lin, L. S. Hollister, C. L. Andronicos, V. V. Distler, M. P. Eddy, A. Kostin, V. Kryachko, G. J. MacPherson, W. M. Steinhard, M. P. Yudovskaya, and L. Steinhard, *Sci. Rep.* **5**, 1–5 (2015).
18. G. T. de Laissardiere, D. Nguyen-Manh, and D. Mayou, *Prog. Mater. Sci.* **6**, 679–788 (2005).
19. I. Chumak, K. W. Richter, H. Ipsen, *Intermetallics* **11**, 1416–1424 (2007).
20. L. Zhang, Y. Du, H. Xu, C. Tang, H. Chen, and W. Zhang, *J. Alloys Compd.* **1–2**, 129–135 (2008).
21. U. Lemmerz, B. Grushko, C. Freiburg, and M. Jansen, *Philos. Mag. Lett.* **3**, 141–146 (1994).
22. B. Grushko and K. Urban, *Philos. Mag. B* **5**, 1063–1075 (1994).
23. B. Grushko and T. Velikanova, *Comput. Coupling Ph. Diagr. Thermochem.* **31**, 217–232 (2007).
24. B. O. Trembach, M. G. Sukov, V. A. Vynar, I. O. Trembach, V. V. Subbotina, O. Yu. Rebrov, O. M. Rebrova, and V. I. Zakiev, *Metallofiz. Noveishie Tekhnologii* **4**, 493–513 (2022).
25. I. M. Spiridonova, E. V. Sukhovaya, and V. P. Balakin, *Metallurgia* **2**, 65–68 (1996).
26. V. A. Dzenzerskii, S. V. Tarasov, Y. I. Kazacha, S. V. Shnurovoi, and V. A. Ivanov, *Russ. Metall.* **11**, 946–951 (2015).
27. O. V. Sukhova and Y. V. Syrovatko, *Metallofiz. Noveishie Tekhnologii* **9**, 1171–1185 (2019).
28. Y. Chabak, V. Efremenko, V. Zurnadzhy, V. Puchý, I. Petryshynets, B. Efremenko, V. Fedun, K. Shimizu, I. Bogomol, V. Kulyk, and D. Jakubéczyová, *Met.* **12**, 218 (2022).
29. O. V. Sukhova, *Metallofiz. Noveishie Tekhnologii* **7**, 1001–1012 (2009).
30. V. A. Dzenzerskii, V. F. Bashev, S. V. Tarasov, V. A. Ivanov, A. A. Kostina, and S.V. Korpach, *Inorg. Mater.* **2**, 140–144 (2014).
31. I. M. Spyridonova, O. V. Sukhova, and G. V. Zinkovskij, *Metall. Min. Ind.* **4**, 2–5 (2012).
32. Y. Zhang, K. Shimizu, X. Yaer, K. Kusumoto, and V. G. Efremenko, *Wear* **390–391**, 135–145 (2017).
33. E. V. Sukhovaya, *J. Superhard Mater.* **5**, 277–283 (2013).

34. B. Trembach, A. Grin, V. Subbotina, V. Vynar, S. Knyazev, V. Vakiev, I. Trembach, and O. Kabatskyi, *Tribol. Ind.* **3**, 452–464 (2021).
35. O. V. Sukhova and Y. V. Syrovatko, *Metallofiz. Noveishie Tekhnologii* **33**, 371–378 (2011).
36. P. A. Belonozhko, M. M. Zhechev, and S. V. Tarasov, *Sov. Appl. Mech.* **7**, 683–688 (1986).
37. B. Trembach, A. Grin, N. Makarenko, S. Zharikov, I. Trembach, and O. Markov, *J. Mater. Res. Technol.* **5**, 10520–10528 (2020).
38. O. V. Sukhova, *Phys. Chem. Solid State* **1**, 110–116 (2021).
39. H. Bitterlich, W. Loeser, and L. Schultz, *J. Phase Equilibria Diffus.* **4**, 301–304 (2002).
40. R. Rablbauer, G. Frommeyer, and F. Stein, *Mater. Sci. Eng. A* **1–2**, 301–307 (2003).
41. B. H. Zeifert, J. Salmones, J. A. Hernandez, R. Reynoso, N. Nava, E. Reguera, J. G. Cabanas-Moreno, G. Aguilar-Rios, and J. Radioanal. Nucl. Chem. **3**, 637–639 (2000).
42. G. Sauthoff, *Intermetallics* **9–11**, 1101–1109 (2000).
43. K. Niihara, *J. Mater. Sci. Lett.* **2**, 221–223 (1983).
44. D. J. Skinner and M. Zedalis, *Scr. Metall. Mater.* **11**, 1783–1785 (1988).
45. J. Pokluda and P. Sandera, *Micromechanisms of Fracture and Fatigue*, Springer, London, 2010.
46. A. Pineau, A. A. Benzerga, and T. Pardoen, *Acta Mater.* **107**, 424–483 (2016).
47. T. A. Ring, P. Feeney, D. Boldridge, J. Kasthurirangan, S. Li, and J. A. Dirksen, *J. Electrochem. Soc.* **3**, 239–248 (2007).
48. G. V. S. Murthy, A. K. Ray, R. K. Minz, and N. K. Mukhopadhyay, *J. Mater. Sci. Lett.* **18**, 255–258 (1999).